



Harmonic generation from gold nanolayers: bound and hot electron contributions to nonlinear dispersion

L. RODRÍGUEZ-SUNÉ,^{1,*}  J. TRULL,¹ C. COJOCARU,¹  N. AKOZBEK,² D. DE CEGLIA,³ M. A. VINCENTI,⁴  AND M. SCALORA⁵

¹Department of Physics, Universitat Politècnica de Catalunya, Rambla Sant Nebridi 22, 08222 Terrassa, Spain

²AEgis Technologies Inc., 401 Jan Davis Dr., Huntsville, Alabama 35806, USA

³Department of Information Engineering – University of Padova, Via Gradenigo 6/a, 35131 Padova, Italy

⁴Department of Information Engineering – University of Brescia, Via Branze 38, 25123 Brescia, Italy

⁵Aviation and Missile Center, US Army CCDC, Redstone Arsenal, AL 35898-5000, USA

*laura.rodriiguez.sune@upc.edu

Abstract: Understanding how light interacts with matter at the nanoscale is pivotal if one is to properly engineer nano-antennas, filters and other devices whose geometrical features approach atomic size. We report experimental results on second and third harmonic generation from 20 nm- and 70 nm-thick gold layers, for TE- and TM-polarized incident light pulses. We discuss the relative roles that bound electrons and an intensity dependent free electron density (hot electrons) play in third harmonic generation. While planar structures are generally the simplest to fabricate, metal layers that are only a few nanometers thick and partially transparent are almost never studied. Yet, transmission offers an additional reference point to compare experimental measurements with theoretical models. Our experimental results are explained well within the context of the microscopic hydrodynamic model that we employ to simulate second and third harmonic conversion efficiencies. Using our experimental observations we estimate $|\chi_{1064nm}^{(3)}| \approx 10^{-18} \text{ (m/V)}^2$, triggered mostly by hot electrons.

© 2021 Optical Society of America under the terms of the [OSA Open Access Publishing Agreement](#)

1. Introduction

Currently, nanostructures are routinely fabricated and integrated in different photonic devices for a variety of purposes and applications. At the nanoscale, which we interpret to mean that material features may be only a few atomic diameters in size, light-matter interactions can display new phenomena, and conventional approximations may not always be applicable. This is the case for processes like second harmonic generation (SHG) and third harmonic generation (THG). Traditionally, SHG and THG have been studied under phase-matched conditions, primarily to improve efficiency in bulk, optically thick materials (hundreds of microns or millimeters) with high nonlinearities and low material absorption across a spectral range that includes the pump and its harmonics. Under these circumstances, the leading nonlinear polarization term corresponds to the bulk contribution from the nonlinear potential described by dipolar second and third order nonlinear susceptibility tensors ($\chi^{(2)}$ and $\chi^{(3)}$). However, at the nanoscale and under pulsed illumination, the effective $\chi^{(2)}$ and $\chi^{(3)}$ may not coincide with their bulk, local counterparts, and may depend on pump depletion, pulse duration and on the type of nonlinearities that are triggered and their associated linear and nonlinear dispersions. In addition, contributions to the nonlinear polarizations arising from electric quadrupole-like and magnetic sources should also be taken into account.

Interest in the nonlinear optical properties of metals arches back to the beginning of nonlinear optics, is still a subject of debate, and is now more relevant than ever insofar as nano-plasmonics

is concerned. Most models currently rely on assigning effective surface and volume $\chi^{(2)}$ for SHG, and an effective volume $\chi^{(3)}$ to describe THG. Ultimately, most theoretical predictions appear to accurately describe the general shape of the angular dependence of the SH signal, but fail in describing the observed amplitude. From a historical point of view, it was pointed out in Ref. [1] that in centrosymmetric media, where bulk $\chi^{(2)}$ vanishes, SHG arises from a magnetic dipole term and from an electric quadrupole-like contribution. Later, in Ref. [2], it was shown that the quadrupole source term was equivalent to a nonlinear surface contribution, and it was proposed that SHG in metals may be explained by considering separate bulk and surface contributions having different weights associated with free electron dynamics. Early experimental evidence of SHG in metals may be found in Ref. [3], where reflected SHG was measured from a silver (Ag) mirror. In Refs. [4] and [5] experimental results of reflected SHG were reported for Ag and gold (Au) mirrors. Additional theoretical and experimental studies followed, a small sample of which may be found in Refs. [6–8], where the main approach is to separate and distinguish between surface and volume contributions. For example, based on the idea of identifying surface and volume sources, in Ref. [9] the magnitude and relative phase of second-order susceptibility tensor elements may be determined for thin-film metal samples of silver, gold, copper, aluminum and tantalum. As another example, in Ref. [10] SHG is reported in diffraction from arrays of symmetric Au nanoparticles, while SHG from single Au elliptical nanoparticles is experimentally investigated in Ref. [11]. Other experimental studies of SHG from Au are reported in Refs. [12] and [13]. Third order nonlinearities have also been studied in a variety of Au samples in various geometries [14–19]. In all cases, however, the predictions of THG results are reconciled with experimental results by assuming an effective bulk $\chi^{(3)}$, without specifying its origin.

As mentioned above, most current theoretical models of SHG rely on the introduction of phenomenological or effective surface and bulk parameters that generally lack a detailed, microscopic, dynamical description of light propagation and light-matter interactions. Here, we present experimental measurements of the angular dependence of SHG and THG in transmission and reflection from 20 nm- (transparent) and 70 nm-thick (opaque) Au nanolayers deposited on a fused silica substrate. These experimental observations are compared with numerical simulations based on a theoretical model that embraces full-scale, time-domain coupling of matter to the macroscopic Maxwell's equations. Our approach consists in formulating a microscopic, hydrodynamic model in order to understand linear and nonlinear optical properties of metals by accounting for competing surface, magnetic, and bulk nonlinearities arising from both free (conduction) and bound (valence) electrons. Just as importantly, our model preserves linear and nonlinear material dispersions, nonlocal effects, and the influence of hot electrons, i.e. electrons that may be temporarily excited from the valence into the conduction band, thus causing a transient increase of the free electron density. This model is adapted and applied anew based on previous work reported in Refs. [20–23], where it is described in details. Application of Newtonian dynamics to free and bound electrons leads to the following simultaneous material equations of motion in three spatial coordinates and time:

$$\begin{aligned} \ddot{\mathbf{P}}_f + \tilde{\gamma}_f \dot{\mathbf{P}}_f = & \frac{e^2 \lambda_0^2 n_{0f}}{m_0^* c^2} \mathbf{E} + \tilde{\Lambda} (\mathbf{E} \cdot \mathbf{E}) \mathbf{E} - \frac{e \lambda_0}{m_0^* c^2} (\nabla \cdot \mathbf{P}_f) \mathbf{E} + \frac{e \lambda_0}{m_0^* c^2} \dot{\mathbf{P}}_f \times \mathbf{H} \\ & + \frac{3E_F}{5m_0^* c^2} \left[\nabla (\nabla \cdot \mathbf{P}_f) + \frac{1}{2} \nabla^2 \mathbf{P}_f \right] - \frac{1}{n_{0f} e \lambda_0} \left[(\nabla \cdot \dot{\mathbf{P}}_f) \dot{\mathbf{P}}_f + (\dot{\mathbf{P}}_f \cdot \nabla) \dot{\mathbf{P}}_f \right] \end{aligned} \quad (1)$$

$$\begin{aligned} \ddot{\mathbf{P}}_{bj} + \tilde{\gamma}_{bj} \dot{\mathbf{P}}_{bj} + \tilde{\omega}_{0,bj}^2 \mathbf{P}_{bj} - \tilde{\beta} (\mathbf{P}_{bj} \cdot \mathbf{P}_{bj}) \mathbf{P}_{bj} = & \frac{n_{0,b} e^2 \lambda_0^2}{m_{bj}^* c^2} \mathbf{E} + \frac{e \lambda_0}{m_{bj}^* c^2} (\mathbf{P}_{bj} \cdot \nabla) \mathbf{E} \\ & + \frac{e \lambda_0}{m_{bj}^* c^2} \dot{\mathbf{P}}_{bj} \times \mathbf{H} \end{aligned} \quad (2)$$

\mathbf{P}_f and \mathbf{P}_{bj} are free and bound electron polarizations, respectively. The derivation of Eqs. (1) and (2) is detailed in Refs. [20–23], but in what follows we provide a summary of the most salient points. The description of the motion of free electrons in Eq. (1) begins with Newton's second law for a single point charge, (hence our use of the word microscopic) followed by the definition of a macroscopic current density $\mathbf{J} = nev = \dot{\mathbf{P}}$ that leads to the usual Drude model. $n = n(\mathbf{r}, t)$ is charge density, e the electronic charge, and \mathbf{v} is the electron's velocity. Allowing for the free motion of charges inside and on the surface of the material implies that the total charge density is conserved, i.e. $\dot{n}(\mathbf{r}, t) = \frac{1}{e} \nabla \cdot \mathbf{J}$, or $n(\mathbf{r}, t) = n_0 + \frac{1}{e} \nabla \cdot \mathbf{P}$, where n_0 is the charge density with no applied field. The local charge density may change as a function of time, so that $\dot{\mathbf{P}} = \dot{\mathbf{J}} = \dot{n}e\mathbf{v} + ne\dot{\mathbf{v}}$, where $\dot{\mathbf{v}} = \frac{d\mathbf{v}}{dt} = \frac{\partial \mathbf{v}}{\partial t} + \mathbf{v} \cdot \nabla$ is a full derivative that gives rise to convective forces. The Drude model, which usually contains a phenomenological damping term and only the electric component of the force ($\dot{\mathbf{P}}_f + \tilde{\gamma}_f \mathbf{P}_f = \frac{e^2 \lambda_0^2 n_{0f}}{m_0^* c^2} \mathbf{E}$), is augmented by the intrinsically nonlinear magnetic Lorentz force ($\frac{e\lambda_0}{m_0^* c^2} \dot{\mathbf{P}}_f \times \mathbf{H}$), and by pressure and viscosity (nonlocal) terms ($\frac{3E_F}{5m_0^* c^2} \left(\nabla (\nabla \cdot \mathbf{P}_f) + \frac{1}{2} \nabla^2 \mathbf{P}_f \right)$) that act mostly on particles that are located near the surface of the material or across material discontinuities. E_F is the Fermi energy, and m_0^* is the free electron's effective mass. If the instantaneous, free electron density is allowed to vary as a function of applied intensity, one may define $n(\mathbf{r}, t) = n_0 + \frac{1}{e} \nabla \cdot \mathbf{P} + \tilde{\Lambda} (\mathbf{E} \cdot \mathbf{E}) \mathbf{E}$. $\tilde{\Lambda}$ is a simplified, scaled coefficient that generally depends on the equilibrium free electron plasma frequency, conductivity (which is also a function of wavelength), temperature, and pulse duration [23], as exemplified by the two-temperature model [24]. For simplicity we assume that $\tilde{\Lambda}$ is a constant.

Equation (2) describes the behavior of bound electrons, i.e. electrons that at low light intensities typically are not allowed to leave atomic sites. In a metal like Au, one free (s-shell) and two bound (p-shell) electron species generally suffice to describe the local, linear dielectric permittivity down to a wavelength of approximately 200 nm. For simplicity, each Lorentz species is characterized by a third order, isotropic nonlinearity $\mathbf{P}_{bj} = -\tilde{\beta} (\mathbf{P}_{bj} \cdot \mathbf{P}_{bj}) \mathbf{P}_{bj}$, where the scaled coefficient $\tilde{\beta} \approx \left(\omega_{0,b1}^2 + \omega_{0,b2}^2 \right) \lambda_0^2 / \left(2L^2 n_{0b}^2 e^2 c^2 \right)$ may be derived in a straightforward manner for a nonlinear, two-dimensional oscillator model. $\omega_{0,b1}$ and $\omega_{0,b2}$ are the two resonance frequencies for the two, chosen bound electron species, L the lattice constant, n_{0b} the bound electron density, $\lambda_0 = 1 \mu\text{m}$ is a convenient reference wavelength chosen in the range of interest, and c is the speed of light in vacuum. In our case, $n_{0b} \sim 5.8 \cdot 10^{22} \text{ cm}^{-3}$ (similar to the free electron density, since each atom yields one free electron, although lower d-shell electrons may also contribute at short-enough wavelengths [25]), the lattice constant $L \sim 3 \cdot 10^{-8} \text{ cm}$, while the two resonance frequencies $\omega_{0,bj} \approx 10^{16} \text{ s}^{-1}$ combine to yield an average resonance wavelength between 300 and 400 nm. As a result, atomic size, crystal structure, and linear oscillator parameters effectively predetermine the dimensionless coefficient $\tilde{\beta} \approx 10^{-8}$, which governs *all* third order effects triggered by the background crystal, i.e. bound electrons, including self-phase modulation, nonlinear absorption, and THG power conversion efficiencies. We note that the lattice constant L represents the maximum allowed extension of a classical spring. However, if we recognize L as a classical representation of electronic orbital radii, then L may vary between 1 Å and 3 Å, a variation that may substantially affect the magnitude of $\tilde{\beta}$.

A cursory examination of Eqs. (1) and (2) reveals that electrons are excited into the conduction band at a rate that depends on incident power density and the magnitude of $\tilde{\Lambda}$, which we assume to be constant. The magnitude of $\tilde{\Lambda}$ may vary substantially, depending on the exact state of the system, incident pulse duration and peak power density. Therefore, third order effects such as THG may be triggered by either or both free and bound electrons. It turns out that our measured efficiencies suggest that the TH signal originates mostly from hot electrons. To our knowledge, the model exemplified by Eqs. (1) and 2 has never before been used in this context, and is unique in several additional respects. For more details on the basic foundations of the model we refer the

reader to Refs. [20–23]. In addition, the reader should consult Ref. [26], where a discussion may be found on the theoretical aspects related to contributions from smooth charge densities arising from electron cloud spill-out. These equations are solved simultaneously together with the macroscopic Maxwell's equations, where the total polarization is the vectorial sum of all polarization components. The spatial and temporal derivatives in Eqs. (1) and (2) are carried out with respect to the following scaled coordinates: $\xi = z/\lambda_0$, $\zeta = y/\lambda_0$, and $\tau = ct/\lambda_0$, where λ_0 is the reference wavelength. The fields are assumed to be invariant along the transverse x -direction. In summary, SHG arises mostly via Eq. (1), although Eq. (2) (the j counter in Eq. (2) indicates multiple bound electron species) is also a source of SHG. THG on the other hand is triggered by both Eqs. (1) and (2), mostly by the terms proportional to $\tilde{\beta}$ and $\tilde{\Lambda}$.

2. Samples and experimental setup

The Au films were deposited from an Au target using a magnetron sputtering system. The DC target power was 100 W and deposition pressure 3 mTorr. The films were analyzed with both a spectrophotometer and spectroscopic ellipsometer for thickness calibration and optical constants. We performed the experiments in a set-up capable of measuring both transmitted and reflected SH and TH signals generated by the pump as it traverses the Au nanolayers. A schematic representation of this set-up is shown in Fig. 1. Two different sources were used in our experiments. The first one was a Ti:Sapphire oscillator at 800 nm (Coherent - MIRA), emitting 140 fs pulses at 76 MHz repetition rate, with a CW output average power of 1.7 W, corresponding to approximately 22 nJ/pulse. The second source was a pulsed fiber laser (FYLA PS50) emitting a train of 13 ps pulses at 1064 nm, with a CW average output power of 2 W at 1 MHz repetition rate, delivering pulses of 2 μ J/pulse. The polarization (TE or TM) of the fundamental beam (FF) incident on the sample was controlled using a half-wave plate. Any possible SH and TH signals arising from different optical components (lenses, mirrors, etc.) placed along the set-up before the sample were removed by spectral filters. To obtain the desired fundamental beam intensities on the sample in the range of 1-2 GW/cm², we focused the fundamental beam at the sample plane by means of plano-convex lenses with focal length $f=200$ mm for the SH measurements, and $f=100$ mm for the TH experiments. The sample was mounted on a rotary support arm that ensures precise control of the FF incident angle, allowing measurements of the SH or TH signals as a function of the fundamental beam angle of incidence. The most critical part of the setup is the detection arm, since the expected power conversion efficiencies are in the range 10^{-8} - 10^{-11} . Immediately after the sample, a filter attenuating the FF radiation was used, thus avoiding any potential SH or TH generation from the surfaces of the optical elements in this part of the set-up. An anti-reflection coated lens with focal length $f=100$ mm was used to collimate the beam after the sample, and a polarizer served to analyze the polarization state of the SH or TH generated fields. In order to detect the faint SH or TH signals arising from the Au samples, it was crucial to separate them from the residual fundamental beam. To this end, we used a prism and a blocking edge to separate and obscure the remaining fundamental field radiation from the SH or TH path. Finally, a photomultiplier tube is used to detect the harmonic signals, on which we place a narrow-band spectral filter having a 20 nm band pass transmission around either the SH or the TH wavelength.

For a more accurate detection, the signal reaching the photomultiplier is modulated in different ways, depending on the laser source. For the femtosecond pulses at 800 nm and at 76 MHz repetition rate, we use a mechanical chopper modulating the fundamental signal at typical frequencies of the order of 100 Hz with a duty cycle of 50%. The picosecond source at 1064 nm can be modulated so it delivers a train of N pulses separated by 1 μ s (1 MHz) which are repeated at a rate of 1 kHz. In this way we can integrate on the photomultiplier signal measurement the response of N pulses and obtain a larger signal. The entire detection system is mounted on a rotary platform that allows us to precisely set the detection angle and to take measurements in

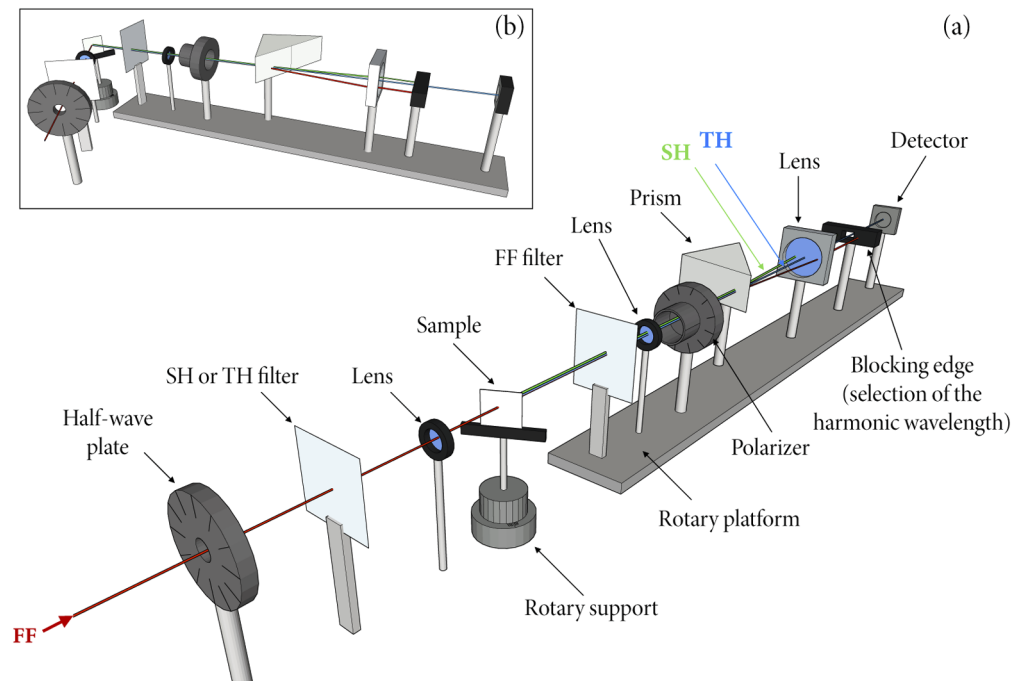


Fig. 1. Set-up developed to measure SH and TH signals generated when light tuned at 800 nm or 1064 nm interacts with an Au nanolayer. The detection system is mounted on a rotary platform so measurements can be taken in transmission (a) and in reflection (b).

transmission and in reflection, as shown in Fig. 1(a) and Fig. 1(b), respectively. Our set-up is able to detect SH and TH signals having power conversion efficiencies of order 10^{-8} down to 10^{-14} . We carried out a detailed calibration procedure to accurately estimate the efficiency of a given process as the ratio between the SH or TH intensity generated in transmission or reflection, and the total peak pump pulse intensity just before the sample. The calibration procedure also included the measurement of possible harmonic signals coming from the blank substrate of fused silica.

3. Experimental and theoretical results

Transmitted and reflected SH efficiencies are measured at a fixed wavelength as functions of fundamental incident angle for two different samples of 20 nm- and 70 nm-thick Au layers. The generated SH signals at 532 nm and 400 nm are recorded for incident pulses having carrier wavelengths tuned to 1064 nm (pulse duration ~ 13 ps) and 800 nm (pulse duration ~ 140 fs), respectively. In either case the simulations are carried out using 100 fs pulses. Barring the intervention of additional physical phenomena, like slow nonlinear thermal effects, the spectral response converges rapidly as a function of incident pulse duration. THG was measured by illuminating the 20 nm-thick Au layer with the pulsed 1064 nm source, which generates a TH field at 355 nm.

In Fig. 2 we show the simulated spectral SH response in reflection and transmission as a function of incident carrier wavelength for both 20 nm- and 70 nm-thick gold layers, at a fixed 55° angle of incidence. Transmitted SHG for the 70 nm layer was below the detection limit and is omitted. For each simulation point shown in Fig. 2, the incident pump field consists of a pulse approximately 100 fs in duration. At longer wavelengths both metal layers act increasingly

as mirrors, as the real part of the dielectric constant becomes progressively more negative, a fact that leads to an enhanced, nonlinear surface response. The relative importance of surface and volume sources changes as a result of varying degrees of penetration depth, and peak SH response is expected to occur at different angles of incidence.

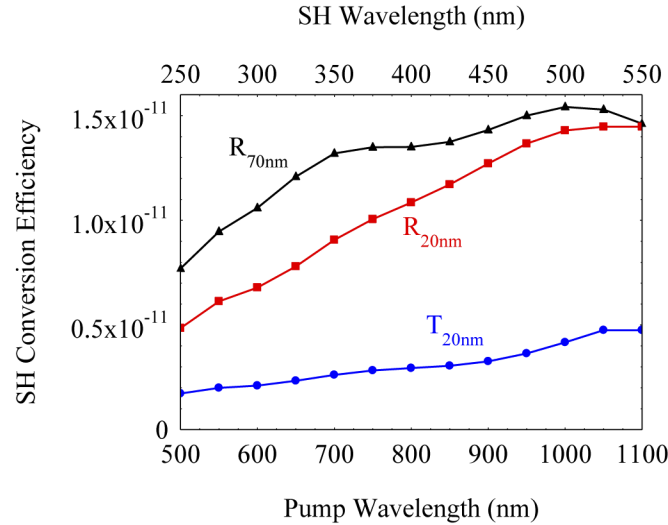


Fig. 2. Calculated SHG conversion efficiency vs. incident wavelength for 20 nm- and 70 nm-thick gold layers. Transmitted SHG efficiency for the 70 nm-thick layer is negligible and is not shown. 100 fs pulses are incident at 55° , and have peak power density of approximately 1 GW/cm^2 . We assume free and bound electron masses and densities are $m_{\text{free}} = m_{\text{bound}} = m_e$, and $n_b \sim 5.8 \cdot 10^{22} \text{ cm}^{-3}$, respectively.

In Fig. 3 we plot and compare experimentally measured and predicted transmitted SHG efficiencies at 800 nm and 1064 nm fundamental wavelengths, respectively, as functions of the angle of incidence for the 20 nm-thick Au layer. The agreement between predicted and measured values is good and occurs notwithstanding the fact that simulations are carried out using incident 100 fs pulses in both instances. This confirms that rapid convergence is achieved as a function of incident pulse duration for flat structures that display no geometrical spectral features. It is evident that experimental and theoretical results agree well in both cases, in shape, amplitude, and peak locations. At longer wavelengths, the main peak shifts to larger angles, field penetration depth decreases and surface charge discontinuities, exemplified by Coulomb $\left(-\frac{e\lambda_0}{m_0^*c^2} (\nabla \cdot \mathbf{P}_f) \mathbf{E}\right)$ and convective $\left(-\frac{1}{n_0 f e \lambda_0} \left[(\nabla \cdot \dot{\mathbf{P}}_f) \dot{\mathbf{P}}_f + (\dot{\mathbf{P}}_f \cdot \nabla) \dot{\mathbf{P}}_f \right] \right)$ terms, increase and become the main source of SHG, although the magnetic contribution encompasses both nonlinear surface and volume currents.

In Fig. 4 we show measured and predicted angular dependence of transmitted and reflected SHG conversion efficiencies from the 20 nm-thick gold sample for 800 nm incident wavelength. Measurements and simulations agree remarkably well, including the ratio of maximum reflected and transmitted efficiencies, and the relative angular positions of the maxima. We emphasize that we have not assumed any effective surface or volume nonlinearities to explain our experimental results. Instead, we rely completely on knowledge of approximate free electron mass and density, which may be ascertained by various means, and incident peak power density. These are the only free parameters in the calculations, which lead to unprecedented, objective qualitative and quantitative agreement between theory and experimental results of SHG from metal structures.

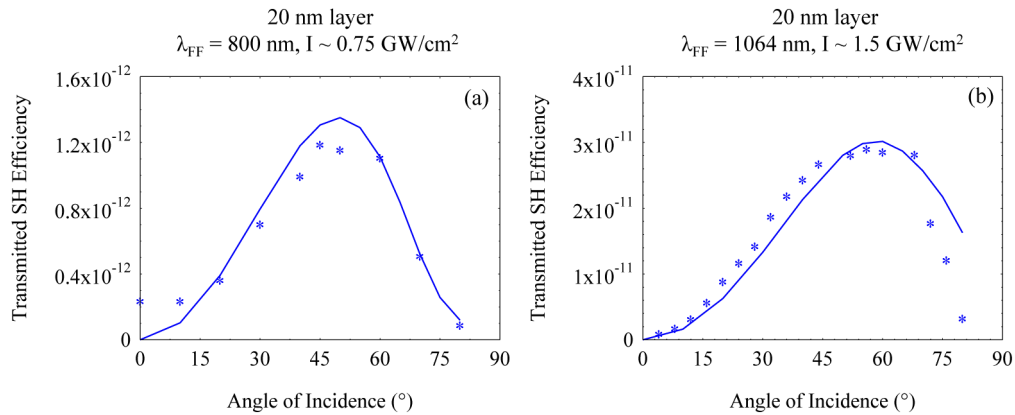


Fig. 3. Measured (blue * markers) and simulated (solid blue curves) of transmitted SHG efficiency as a function of incident angle for the 20 nm-thick Au layer when the incident field is tuned at (a) 800 nm, with peak power density of approximately 0.75 GW/cm^2 , and (b) 1064 nm and peak power density of order 1.5 GW/cm^2 .

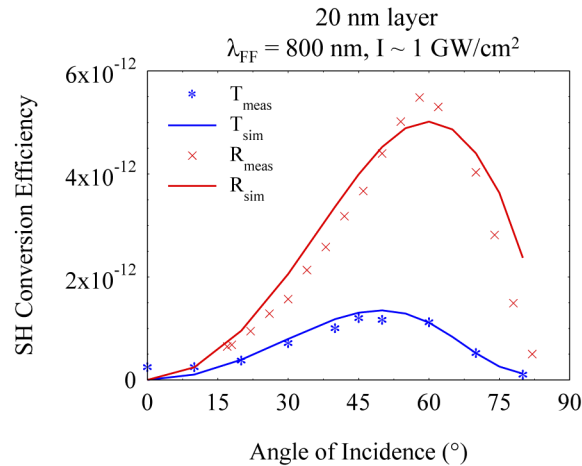


Fig. 4. Measured (blue * and red x symbols) and corresponding simulated (solid blue and red curves) of transmitted and reflected SHG efficiencies, as indicated, as functions of incident angle for the 20 nm-thick Au layer when the incident field is tuned at 800 nm. The transmission curves are identical to those in Fig. 3.

In Fig. 5 we plot reflected SHG power conversion efficiencies as functions of incident angle for 800 nm and 1064 nm pulsed laser sources for the 70 nm-thick gold layer. Transmission is negligible in both cases. We remark that once again experimental and theoretical results agree quite well qualitatively and quantitatively. Peak SHG performance shifts from $\sim 60^\circ$ at 800 nm, to $\sim 75^\circ$ at 1064 nm, reflecting changes in field penetration depth in the two different spectral ranges.

As outlined above, a system described by combined Drude and Lorentz electrons illuminated by a pulsed pump laser source has at least two main THG sources: interband transitions (Lorentz resonances, with nonlinear interactions governed by the parameter $\tilde{\beta}$) and hot electrons, whose relative strength is determined by $\tilde{\Lambda}$. Other types of nonlinearities, such as a slower thermal response, may be controlled and excluded simply by reducing pulse repetition rate, which we have done in our experiment so as to limit the kinds of nonlinearities active in our system. Any additional nonlinearity triggered on a time scale slower compared to the relatively fast electronic

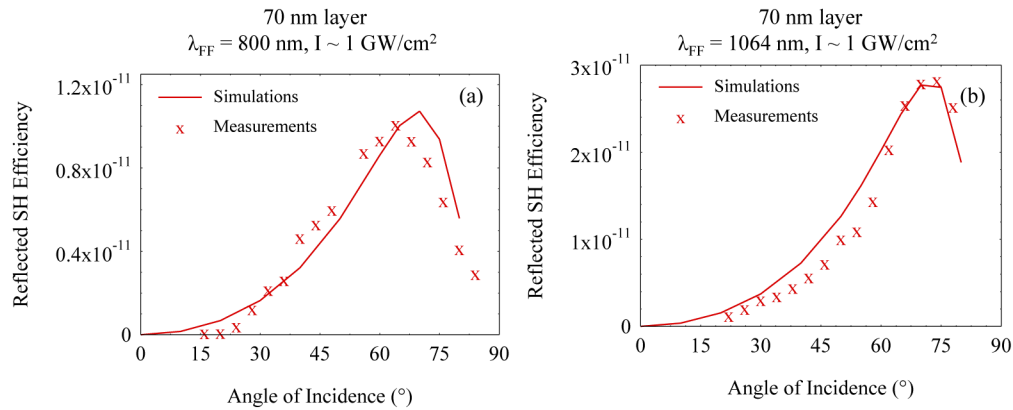


Fig. 5. Measured (red x symbols) and simulated (solid red curves) of reflected SHG efficiency as a function incident angle for the 70 nm-thick Au layer when the carrier wavelength is (a) 800 nm, and (b) 1064 nm. We slightly adjust incident peak power density, effective electron mass and density and reproduce quite well the amplitudes and approximate peak locations in both cases.

responses that we consider may be easily included by introducing appropriate terms in either or both Eqs. (1) and (2), depending on the origin of the process. Therefore, as written, Eqs. (1) and (2) fully account for the mixing of linear and nonlinear material dispersions due to the combined action of free and bound electrons, with modifications induced by the presence of nonlocal and magnetic effects.

In Fig. 6 we plot the predicted, reflected THG spectral response for 100 fs pulses incident at 55° . The transmitted signal is predicted to display similar behavior. In this example the parameters are chosen arbitrarily so that each nonlinear contribution yields similar THG conversion efficiency when the other is turned off. Then we combine them together to ascertain the interplay between these two different TH sources. The figure suggests that separately, each type of third order nonlinearity yields qualitatively and quantitatively a similar response, with a TH peak for pump (TH) wavelength of ~ 600 nm (200 nm). However, their combined response redshifts the TH peak. This prediction runs counter to intuition because an increased free electron density should blueshift the plasma frequency, with expectedly similar outcome for the TH peak. It is obvious that the two components interfere and conspire to instead redshift the peak, an effect that encapsulates a cautionary tale for any experimental result that may be cavalierly extrapolated without the benefit of proper assumptions and theoretical support.

The transmitted angular dependence of THG was recorded from the 20 nm-thick gold layer using the 1064 nm laser source. The repetition rate was varied to insure thermal effects were not excited. Measured and simulated THG power conversion efficiencies are shown in Fig. 7. The blue * markers denote the transmitted, TM-polarized TH for a TM-polarized incident field. The red x markers represent the TE-polarized TH signal for a TE-polarized pump. The angular dependence of THG is different compared to SHG because the inherent nonlinearity in this case is triggered by the bulk, with conversion efficiencies of order of 10^{-8} . A scaled coefficient $\tilde{\beta} = 10^{-8}$ alone yields conversion efficiencies of order 10^{-11} , clearly inadequate to explain our observations. Instead, what is required to reproduce the conversion efficiencies that we observe is the introduction of $\tilde{\Lambda} \approx 3 \cdot 10^{-8}$. Using a harmonic oscillator model [27], it can be shown that this corresponds to $\chi_{1064nm}^{(3)} \approx -3.7 \cdot 10^{-18} + i2.1 \cdot 10^{-19} \text{ (m/V)}^2$, and $\chi_{355nm}^{(3)} = -1.5 \cdot 10^{-19} + i1.1 \cdot 10^{-20} \text{ (m/V)}^2$. Oscillatory behavior at small angles is likely due

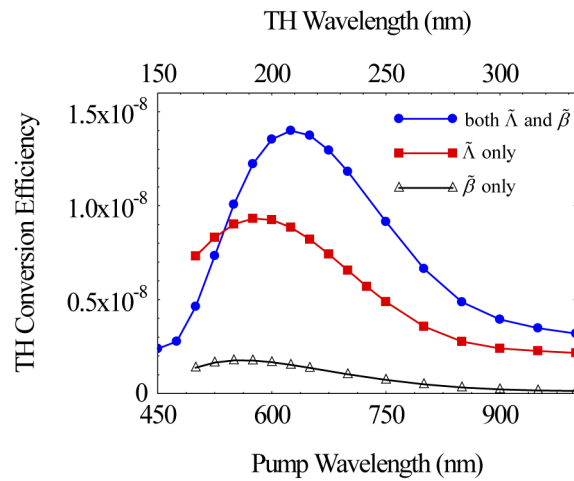


Fig. 6. Prediction of reflected THG conversion efficiency vs. wavelength for pump pulses incident at 55° .

to the sensitivity of the set-up [28]. Nevertheless, the figure suggests that both efficiency and angular response are well-predicted by our model.

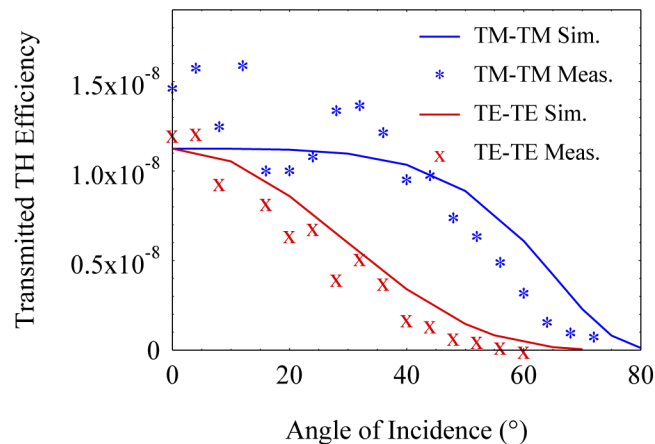


Fig. 7. Measured (blue * and red x symbols) and simulated (solid blue and red curves) transmitted THG efficiency as a function of incident angle for TM- and TE-polarized incident pump pulses tuned to 1064 nm, incident on a 20 nm-thick gold layer. In the legend, TM-TM indicates the polarization of pump and generated TH, respectively, and similarly for TE-TE.

4. Conclusion

In conclusion, we have reported experimental observations of SHG and THG in transparent and opaque gold nanolayers. A transparent, 20 nm-thick layer is used to monitor transmitted and reflected SH signals, as the fields carry information about combined surface and volume currents excited on and inside the sample. On the other hand, the opaque, 70 nm-thick gold layer supports mostly surface currents, with reflected conversion efficiencies that are largest at larger angles. We use a hydrodynamic approach to model light-matter interactions, and make no assumptions about effective surface or volume nonlinearities. Instead, we rely on temporal and spatial derivatives and

mere knowledge of the effective electron mass to determine the relative magnitudes of surface and volume contributions. In doing so, we find remarkable agreement with experimental observations. We also report observations of TM- and TE-polarized, transmitted THG from the 20 nm-thick gold layer. We attribute the generated TH signal mostly to hot electron dynamics, and estimate $\chi_{1064nm}^{(3)} \approx -3.7 \cdot 10^{-18} + i2.1 \cdot 10^{-19} \text{ (m/V)}^2$, and $\chi_{355nm}^{(3)} = -1.5 \cdot 10^{-19} + i1.1 \cdot 10^{-20} \text{ (m/V)}^2$. Finally, we note that intensity-driven increases in free electron density do not significantly alter the efficiencies of second order processes.

Funding. Agencia Estatal de Investigación; Army Research Laboratory (W911NF-20-2-0078); Research, Development and Engineering Command (W911NF-18-1-0126).

Acknowledgment. N.A. and M.S. acknowledge discussions with D. D. Smith.

Disclosures. The authors declare no conflicts of interest.

References

1. E. Adler, "Nonlinear optical frequency polarization in a dielectric," *Phys. Rev.* **134**(3A), A728–A733 (1964).
2. S. S. Jha, "Theory of optical harmonic generation at a metal surface," *Phys. Rev.* **140**(6A), A2020–A2030 (1965).
3. F. Brown, R. E. Parks, and A. M. Sleeper, "Nonlinear optical reflection from a metallic boundary," *Phys. Rev. Lett.* **14**(25), 1029–1031 (1965).
4. N. Bloembergen, R. K. Chang, and C. H. Lee, "Second-harmonic generation of light in reflection from media with inversion symmetry," *Phys. Rev. Lett.* **16**(22), 986–989 (1966).
5. N. Bloembergen, R. K. Chang, S. S. Jha, and C. H. Lee, "Optical second-harmonic generation in reflection from media with inversion symmetry," *Phys. Rev.* **174**(3), 813–822 (1968).
6. J. Rudnick and E. A. Stern, "Second-harmonic radiation from metal surfaces," *Phys. Rev. B* **4**(12), 4274–4290 (1971).
7. J. E. Sipe, V. C. Y. So, M. Fukui, and G. I. Stegeman, "Analysis of second-harmonic generation at metal surfaces," *Phys. Rev. B* **21**(10), 4389–4402 (1980).
8. A. Liebsch, "Second-harmonic generation at simple metal surfaces," *Phys. Rev. Lett.* **61**(10), 1233–1236 (1988).
9. D. Krause, C. W. Teplin, and C. T. Rogers, "Optical surface second harmonic measurements of isotropic thin-film metals: Gold, silver, copper aluminum, and tantalum," *J. Appl. Phys.* **96**(7), 3626–3634 (2004).
10. M. D. McMahon, R. Lopez, R. F. Haglund, J. E. A. Ray, and P. H. Bunton, "Second-harmonic generation from arrays of symmetric gold nanoparticles," *Phys. Rev. B* **73**(4), 041401 (2006).
11. M. Zavelani-Rossi, M. Celebrano, P. Biagioni, D. Polli, M. Finazzi, L. Duò, G. Cerullo, M. Labardi, M. Allegrini, J. Grand, and P.-M. Addam, "Near-field second-harmonic generation in single gold nanoparticles," *Appl. Phys. Lett.* **92**(9), 093119 (2008).
12. Y. Zeng, W. Hoyer, J. Liu, S. W. Koch, and J. V. Moloney, "Classical theory for second-harmonic generation from metallic nanoparticles," *Phys. Rev. B* **79**(23), 235109 (2009).
13. F. X. Wang, F. J. Rodríguez, W. M. Albers, R. Ahorinta, J. E. Sipe, and M. Kauranen, "Surface and bulk contributions to the second-order nonlinear optical response of a gold film," *Phys. Rev. B* **80**(23), 233402 (2009).
14. H. B. Liao, R. F. Xiao, J. S. Fu, H. Wang, K. S. Wong, and G. K. L. Wong, "Origin of third-order optical nonlinearity in Au:SiO₂ composite films on femtosecond and picosecond time scales," *Opt. Lett.* **23**(5), 388 (1998).
15. D. D. Smith, Y. Yoon, R. W. Boyd, J. K. Campbell, L. A. Baker, R. M. Crooks, and M. George, "Z-scan measurement of the nonlinear absorption of a thin gold film," *J. Appl. Phys.* **86**(11), 6200–6205 (1999).
16. S. Debrus, J. Lafait, M. May, N. Pinçon, D. Prot, C. Sella, and J. Venturini, "Z-scan determination of the third-order nonlinearity of gold:silica nanocomposites," *J. Appl. Phys.* **88**(8), 4469 (2000).
17. R. West, Y. Wang, and T. Goodson, "Nonlinear absorption properties in novel gold nanostructured topologies," *J. Phys. Chem. B* **107**(15), 3419–3426 (2003).
18. A. I. Rysanyanskiy, B. Palpant, S. Debrus, U. Pal, and A. Stepanov, "Third-order nonlinear-optical parameters of gold nanoparticles in different matrices," *J. Lumin.* **127**(1), 181–185 (2007).
19. R. W. Boyd, Z. Shi, and I. D. Leon, "The third-order nonlinear optical susceptibility of gold," *Opt. Commun.* **326**, 74–79 (2014).
20. M. Scalora, M. A. Vincenti, D. de Ceglia, V. Roppo, M. Centini, N. Akozbek, and M. J. Bloemer, "Second- and third-harmonic generation in metal-based structures," *Phys. Rev. A* **82**(4), 043828 (2010).
21. M. Scalora, M. A. Vincenti, D. de Ceglia, C. M. Cojocaru, M. Grande, and J. W. Haus, "Nonlinear duffing oscillator model for third harmonic generation," *J. Opt. Soc. Am. B* **32**(10), 2129–2138 (2015).
22. L. Rodríguez-Suné, M. Scalora, A. S. Johnson, C. Cojocaru, N. Akozbek, Z. J. Coppens, D. Perez-Salinas, S. Wall, and J. Trull, "Study of second and third harmonic generation from an indium tin oxide nanolayer: influence of nonlocal effects and hot electrons," *APL Photonics* **5**(1), 010801 (2020).
23. M. Scalora, J. Trull, D. de Ceglia, M. A. Vincenti, N. Akozbek, Z. Coppens, L. Rodríguez-Suné, and C. Cojocaru, "Electrodynamics of conductive oxides: Intensity-dependent anisotropy, reconstruction of the effective dielectric constant, and harmonic generation," *Phys. Rev. A* **101**(5), 053828 (2020).
24. S. I. Anisimov, B. L. Kapeliovich, and T. L. Perelman, "Electron emission from metal surface exposed to ultrashort laser pulses," *Sov. Phys. JETP* **39**, 375–377 (1974).

25. H. Ehrenreich and H. R. Philipp, "Optical properties of Ag and Cu," *Phys. Rev.* **128**(4), 1622–1629 (1962).
26. M. Khalid and C. Ciraci, "Enhancing second-harmonic generation with electron spill-out at metallic surfaces," *Commun. Phys.* **3**(1), 214 (2020).
27. R. W. Boyd, *Nonlinear Optics* (Academic Press, 2003).
28. W. K. Burns and N. Bloembergen, "Third-harmonic generation in absorbing media of cubic or isotropic symmetry," *Phys. Rev. B* **4**(10), 3437–3450 (1971).